MJFAS
Malaysian Journal of Fundamental and Applied Sciences

RESEARCH ARTICLE

Rhizomucor miehei Lipase Nanoconjugates for Visualizing Latent Fingermarks on Wet Glass Slides: Bioinformatics, Characterization and Laboratory Assessment

Nik Ihtisyam Majdah Nik Razi[a], Naji Arafat Mahat[a,b,c,d,e*], Aida Rasyidah Azman[a,b,d], Roswanira Abdul Wahab[a,b,d], Habeebat Adekilekun Oyewusi[f,g], Azzmer Azzar Abdul Hamid[h], Norita Nordin[i]

[a]Department of Chemistry, Faculty of Science, Universiti Teknologi Malaysia, 81310 UTM Johor Bahru, Johor, Malaysia; [b]Enzyme Technology and Green Synthesis Research Group, Faculty of Science, Universiti Teknologi Malaysia, 81310 UTM Johor Bahru, Johor, Malaysia; [c]Centre for Sustainable Nanomaterials, Ibnu Sina Institute for Scientific and Industrial Research, Universiti Teknologi Malaysia, 81310 UTM Johor Bahru, Johor, Malaysia; [d]Investigative and Forensic Sciences Research Group, Universiti Teknologi Malaysia, 81310 UTM Johor Bahru, Johor, Malaysia; [e]Centre of Research For Fiqh Forensics and Judiciary, Universiti Sains Islam Malaysia, 71800 Negeri Sembilan, Malaysia; [f]Department of Biosciences, Faculty of Science, Universiti Teknologi Malaysia, 81310 UTM Johor Bahru, Johor, Malaysia; [g]Department of Medical Biochemistry, College of Medicine, Faculty of Basic Medical Sciences, Federal University of Health Sciences Ila-Orangun, Osun State, Nigeria; [h]Department of Biotechnology, Kulliyah of Science, International Islamic University Malaysia, 25200 Kuantan, Pahang, Malaysia; [i]Fingerprint Investigation Unit (D10), Criminal Investigation Department, Forensic Laboratory of Royal Malaysia Police, BT. 8 ½, Jalan Cheras,43200 Cheras Selangor, Malaysia

Abstract Developing latent fingermarks on wet, non-porous substrates presents significant challenges, and conventional Small Particle Reagent (SPR) method often involves toxic components. Existing nanobio-based reagents for fingermark development exhibit a limited fatty acid spectrum. Consequently, investigating the broader ligand specificity of *Rhizomucor miehei* lipase (RML) nanoconjugate (nanobio-based reagent1, NBR-1) as a potential fingermark biosensor is pertinent. Molecular docking analysis determined the binding affinities of NBR-1 for decanoic, palmitic, docosanoic, and stearic acids to be -4.9, -5.5, -6.1, and -6.8 kcal/mol, respectively. Molecular dynamics simulations, assessed *via* root mean square deviation (RMSD), root mean square fluctuation (RMSF), radius of gyration (Rg), hydrogen bond count, and Molecular Mechanics Poisson-Boltzmann Surface Area (MM-PBSA) analysis, confirmed stable complex formation in all cases, evidenced by consistent hydrogen bonding (distances: 2.2–3.4 Å). NBR-1 characterization by Attenuated Total Reflectance-Fourier Transform Infrared spectroscopy revealed that RML immobilization on F-MWCNTs (NBR-1) was evidenced by a shift of the amide C=O stretch from 1640 to 1653 cm^{-1} and by the reduced intensity and broadening of the carboxylate C–O peak at 1256 cm^{-1}, confirming polypeptide chain presence. Field Emission Scanning Electron Microscopy demonstrated the increment in the RML thickness, providing evidence for successful RML molecule attachment to the F-MWCNT surface. Under controlled

***For correspondence:**
naji.arafat@utm.my

Received: 22 July 2025
Accepted: 11 Sept. 2025

laboratory conditions, the synthesized NBR-1 reagent successfully developed latent fingermarks (exhibiting low background noise) on glass slides submerged in water for periods of 7 and 14 days. These empirical findings corroborate the initial bioinformatic predictions. Therefore, the results robustly validate NBR-1 as a promising candidate technology for visualizing latent fingermarks, specifically on water-immersed, wet non-porous surfaces, in forensic contexts.

Keywords: Latent fingermarks, *Rhizomucor miehei* lipase nanoconjugates, nanobio-based reagent, bioinformatics, forensic science.

Introduction

Fingermarks possess inherent evidential significance due to three pertinent properties: their unchanging individual uniqueness, persistence over a person's lifetime, and the existence of standardized ridge pattern classifications [1–3] . Forensic identification of individuals, whether suspects or victims, frequently depends on the examination of latent prints. However, their concealed nature presents inherent challenges for investigators. These difficulties intensify significantly when evidence items (e.g., glassware, knives) have been submerged in aquatic environments [4]. Water exposure degrades fingermarks by dissolving short-chain amino acids [5], while mechanical action and aquatic organisms further disrupt residue integrity [6]. According to definition given by Schönfeld and Wojtczak [7], the total carbon atom numbers from 1 to 6 are classified as short chains, while 7 to 12 as well as 13 and more carbon atoms are regarded as medium and long chains, respectively. Consequently, visualizing such compromised marks often necessitates applying specific reagents (e.g., Small Particle Reagent, SPR). These agents interact primarily with residual water-insoluble components, such as fatty acids, to facilitate detection [8].

The fact that visualization of latent fingermarks using reagents like SPR may require rinsing steps, concerns regarding human toxicity and ecological damage from persistent accumulation of toxic materials in aquatic systems have spurred research into environmentally sustainable fingermarks visualization reagents. This urgency stems from the hazardous components of conventional SPR: white SPR contains titanium dioxide (TiO_2), potentially carcinogenic due to intracellular reactive oxygen species generation [4], while dark SPR contains molybdenum disulphide (MoS_2), linked to respiratory impairment [9,10], skin irritation [11], and adverse ecological interactions in aquatic settings [12]. These metallic compounds are compounded by toxic surfactants/solubilizers: sodium tetradecyl sulfate (STS), classified as Skin Corrosive Category 1B (Skin Corr. 1B, H314), and ethylene glycol monomethyl ether (DEGEE), recently associated with dose, duration, and route-dependent nephrotoxicity [13]. The cumulative, long-term environmental threat posed by these four toxic compounds entering water bodies, particularly *via* effluent from fingermarks processing rinse steps, demands mitigation. Consequently, researchers are increasingly exploring nanobiotechnology as a foundation for developing greener visualization reagents [4].

Within this framework, forensic research by Azman *et al*. [3,4,13] demonstrates significant relevance through their development of a novel, environmentally friendly nanobio-based reagent (NBR). This agent employs *Candida rugosa* lipase (CRL) immobilized onto multi-walled carbon nanotubes (MWCNTs) for potential fingermarks visualization. However, their findings indicate the NBR exhibited greater efficacy on groomed fingermarks compared to natural deposits, with conventional SPR outperforming the NBR in several test scenarios. Gas chromatography analysis [14] underpinned the NBR's visualization mechanism, revealing a predominance of long-chain fatty acids (specifically hexadecanoic acid, C16, and octadecanoic acid, C18) in water-submerged fingermark residues. This presents a functional challenge, as CRL characteristically demonstrates higher catalytic activity towards shorter-chain fatty acids (C4, C8, C10, C12) [15]. The established prevalence of long-chain fatty acids in residues from objects submerged for four weeks [14] suggests a potential limitation in CRL's biosensing efficiency within this NBR formulation. This enzymatic mismatch likely explains the observed instances where SPR demonstrated superior performance relative to the NBR in their investigations [3,13].

Given this rationale, employing lipases exhibiting broader fatty acid specificity than CRL represents a strategic solution for developing versatile, novel, and ecologically sustainable nanobio-based fingermark visualization reagents. *Rhizomucor miehei* lipase (RML) demonstrates particular promise as a biosensing agent for detecting long-chain fatty acids in fingermarks subjected to prolonged aquatic submersion. Its broad substrate range encompassing fatty acids from C10 to C22 [16], combined with robust enzymatic specificity and versatility [16], renders it highly suitable for targeting these residues. Notably, despite RML's well-documented utility across diverse biotechnological applications, its potential for detecting and visualizing latent fingermarks on non-porous surfaces recovered from aquatic environments remains unexplored in the current scientific literature.

Bioinformatics has gained substantial traction in contemporary research, driven by its capacity to synthesize interdisciplinary data from fields including gene therapy [18] and pharmaceutical development [19,20], alongside modeling molecular interactions such as those between fluorescein and nanobio-based reagents [21]. Leveraging these computational advantages, this study's principal aim was to computationally evaluate the novel RML-MWCNTs complex (designated nanobio-based reagent-1, NBR-1) as a fingermark biosensor using molecular docking and molecular dynamics simulations. These analyses specifically probed potential interactions between NBR-1 and characteristic fatty acids present in latent fingermarks deposited on non-porous substrates following aquatic submersion (≤14 days). Experimental validation comprised characterizing NBR-1 *via* Attenuated Total Reflectance-Fourier Transform Infrared Spectroscopy (ATR-FTIR) and Field Emission Scanning Electron Microscopy (FESEM), followed by empirical performance assessment. This study aims to investigate the utility of NBR-1 as a novel, green, nanobio-based reagent for visualizing latent fingermarks on wet non-porous surfaces through a combination of bioinformatics modelling and laboratory validation for proving feasibility of the concept (International Fingerprint Research Group guideline, [22]). The findings establish a foundational basis for advancing NBR-1 within fingermark visualization technologies. This research anticipates in forming future progress toward ecologically sustainable forensic methods by reducing reliance on hazardous compounds and enhancing operational safety for practitioners and ecosystems.

Materials and Methods

This present research investigated the use of NBR-1 as a fingermark detection and visualization technology *via* bioinformatics (molecular docking and molecular simulations), its characterization (using ATR-FTIR and FESEM) and a laboratory assessment of visualized fingermarks. While the acid-functionalized MWCNTs (F-MWCNTs) were purchased from the Usains Holding Sdn Bhd (Universiti Sains Malaysia), RML (≥20,000 U·g) and black SPR were procured from Novozymes (Denmark) and Sirchie (Youngsville, USA), respectively. Materials acquired from QRëC (New Zealand) included acetone (99% purity) and potassium phosphate buffer adjusted to pH 7.0. Research ethics approval was provided by Universiti Teknologi Malaysia's committee, granting approval via reference UTMREC-2025-135.

Bioinformatics

Data Retrieval

The three-dimensional (3D) crystal structures of RML (PDB: 4TGL) was sourced from the Protein Data Bank (https://www.rcsb.org/). The structures of palmitic acid (CID: 985) and docosanoic acid (CID: 8215) were obtained from the PubChem (https://pubchem.ncbi.nlm.nih.gov/). As for the same for stearic acid (CID: 5091), decanoic acid (CID: 2863), ChemSpider (http://www.chemspider.com/) database was used. As suggested by the previous researchers [23], the ligands' .sdf and .mol files were subsequently transformed into .pdb format using Open Babel software version 2.3.1 (https://openbabel.org/) [23].

Molecular Docking

This study employed AutoDock 4.2 [24] and AutoDock Vina ("Vina") [25] for molecular docking to determine energetically favorable orientations between RML and four lipid ligands: C10, C16, C18, and C22. Initial preparation involved reconstructing missing polar and non-polar hydrogens in the Protein Data Bank-derived RML structure, followed by the application of Kollman and Gasteiger charges. During docking scoring, partial atomic charges and binding interactions were calculated using polar hydrogens only. Consequently, for the RML structure, the Kollman and Gasteiger charge computations were performed on the non-polar hydrogens exclusively, while the polar hydrogens were used for the scoring function.

Table 1 represents the information on grid boxes for all four ligands. The specific-site docking approach was utilized for the native substrate, specifically targeting the pocket containing the catalytic triad of RML Serine-144 (Ser144), Aspartic acid-203 (Asp203), and Histidine-257 (His257) [25] in the RML-lipids complexes. During ligand preparation, all hydrogen atoms were incorporated before merging non-polar hydrogens to assign Kollman and Gasteigher charges. Subsequently, the appropriate torsion was utilized to enable conformational flexibility during docking. Subsequent docking simulations deployed AutoDock Vina to predict optimal RML-lipid complexes, prioritizing conformations with minimal binding energy. The complexes were subsequently displayed architecturally using the Discovery Studio Visualiser program (https://discover.3ds.com/discovery-studio-visualizer-download) [28], San Diego: Dassault Systemes, 2016) and the three-dimensional ligand interactions (zoomed view) using PyMOL version 2.6 software.

Table 1 Information of grid boxes for all the four ligands.

NBR-1-lipids complexes	Grid center (Å)	Size of grid box
Decanoic acid (C10)	X:-22.907 Y:17.214 Z: 82.751	X: 18 Y: 16 Z: 14
Palmitic acid (C16)	X: -22.907 Y:17.214 Z: 82.751	X: 22 Y: 20 Z: 20
Stearic acid (C18)	X: -22.94 Y: 16.211 Z: 81.611	X: 18 Y:18 Z:18
Docosanoic acid (C22)	X: -22.907 Y: 17.214 Z: 82.751	X: 22 Y:20 Z: 18

The grid box sizes used were relevant to the sizes of the catalytic triads involves in the specific docking.

Molecular Dynamics (MD) Simulation

RML-ligand complexes underwent MD simulations in GROMACS 5.1.4 (parallel implementation; www.gromacs.org), applying the GROMOS 54a7 forcefield. Initial ligand preparation used Avogadro for hydrogen addition and the Automated Topology Builder (ATB; atb.uq.edu.au) for topology generation. Resultant .itp files and original .pdb geometries were integrated into MD systems. Pre-simulation, RML and fatty acid ligands were combined to form complexes, subsequently solvated in a cubic periodic boundary (1.0 Å edge) with ~177,000 SPC/E water molecules. In order to neutralise the system, 17 solvent molecules were substituted by an equal amount of sodium ions. The system underwent a moderate energy minimization process utilising the leap-frog approach, which involved integrating Newton's equations and applying the steepest descent algorithm. This process continued until the system reached its minimum energy state, which typically occurred after approximately 2000 steps.

The system was subjected to a two-phase equilibration process after energy minimization using the steepest descent algorithm to relax unwanted contacts and reduce potential energy. The first involved a Number of particles, Volume, and Temperature (NVT) ensemble with a constant temperature that was achieved using a thermostat; the second involved a Number of particles, Pressure, and Temperature (NPT) ensemble. Simulations were performed during the production phase under constant conditions of 300K and 1 atm. MD simulations were conducted on each lipase-ligand complex using a time step of 2 fs for a duration of 100 ns in triplicates. The dynamics and stability of each complex were assessed using root mean square deviation (RMSD), root mean square fluctuation (RMSF), radius of gyration (Rg), and the number of hydrogen bonds.

Binding Free Energy Calculations

The Molecular Mechanics Poisson-Boltzmann Surface Area (MM-PBSA) method is a dependable tool for demonstrating the calculations of binding free energy and confirming MD simulation findings. Here, the study utilized the g_mmpbsa tool, which was integrated with the GROMACS package and combined with the Adaptive Poisson-Boltzmann Solver (APBS), to compute the binding free energy of the enzyme-ligand complexes [27]. The aforementioned integrated program offered a comprehensive assessment of the MM-PBSA interaction in order to verify the previous MD simulation findings. The mean of triplicated MM-PBSA calculations for the binding free energy of each protein-ligand complex was computed in a way consistent with previous studies [28,29].

NBR-1 Characterization using ATR-FTIR and FESEM

The Immobilization efficacy of RML on F-MWCNTs was verified via ATR-FTIR (Perkin Elmer Frontier) and FESEM (Hitachi SU8020) characterization of commercial F-MWCNTs and RML-MWCNTs (NBR-1).

For ATR-FTIR, minute amounts of F-MWCNT and NBR-1 samples were individually compressed against the diamond crystal under high-pressure clamping. Spectral acquisition spanned 650–4000 cm^{-1} at 4 cm^{-1} resolution with 16 co-added scans. As for FESEM, it operated at 5 kV and 10 µA. Powdered F-MWCNTs were directly mounted on FESEM stab using a double-sided conductive carbon tape. NBR-1 fingermark on glass coverslips received a thin layer platinum sputter-coating prior to carbon-tape mounting.

Laboratory Assessment of Visualized Fingermarks using NBR-1

Preparation of NBR-1

Following the bioinformatics and characterization studies, the laboratory assessment of the visualize fingermarks by the NBR-1 to support its application as a candidate for forensic visualization technology was attempted. For immobilization, 100 mg F-MWCNT was agitated (150 rpm) for 5 h at room temperature with 7 µL of RML solution (2.344 mg/mL) in 12 mL phosphate buffer (100 mM, pH 7). The mixture underwent refrigerated storage (4°C) pending further use [4].

Donors and Fingermark Deposition

To simulate natural facial touching [29], groomed whole fingermarks from the right thumb-contacted T-zone were collected from two consented healthy Malaysian donors (1 male, 1 female) aged between 21-50 years old, without any mental disabilities and/ or known dangerous infectious diseases (e.g.: AIDS, Covid-19 and Hepatitis). Each donor deposited 20 fingermarks onto different acetone-cleaned glass slides (with a contact period of 3 seconds), bringing the total of 40 fingermarks evaluated during the laboratory assessment. Once deposited fingermarks were left to dry in the air for about 1 minutes prior to submersion in water. Slides mounted on cylindrical plastic meshes with nylon restraints underwent 14-day immersion in stagnant tap water under controlled conditions: pH 7.27–7.81, temperature 26.7–28.8°C, turbidity 0.04–0.26 NTU, dissolved oxygen 7.15–7.92 mg/L. Visualization involved applying 3–5 NBR-1 drops per slide, gentle tap-water rinsing, and quality assessment via the modified-CAST absolute scale [33].

Statistical Analysis

Data analyses were conducted using the UTM-licensed IBM SPSS version 29 software. The data were presented as mean ± standard deviation with 10 replicates for each duration (day-7 and day-14) and gender (male and female). Since the data were normally distributed (as evident by p-values ≥ 0.05 for Shapiro wilk test of normality), comparisons of the quality of the fingermarks between the two intervals as well as between male and female were performed individually using the Independent Sample t-test with the significance level of 0.05. Using the Levene Test for Equality of Variances, the assumption of equal variances was ascertained.

Results and Discussion

Molecular Docking Analysis of Ligand-Protein Interactions

This study assessed the utility of synthesized RML in NBR-1 as a biosensor targeting characteristic fatty acids present in latent fingermarks deposited on submerged objects. As reported by Azman *et al.*, [14], these residues comprise long-chain (C16, C18, C22) and short-chain (C10) fatty acids. Consequently, we examined the binding interactions between RML in NBR-1 and these fatty acid ligands, leveraging the documented broad lipid specificity (C10-C22) of RML [16]. Molecular docking and MD simulations, performed using Autodock 4.2 and Vina, characterized these interactions. Computational predictions were subsequently validated through experimental observation. Hydrogen bonding patterns, particularly with the RML catalytic triad (Ser144, Asp203, His257) [26] and additional residues (Ser82, Tyr28, His143), were analyzed using Discovery Studio Visualizer (Figure 1-4, Table 2).

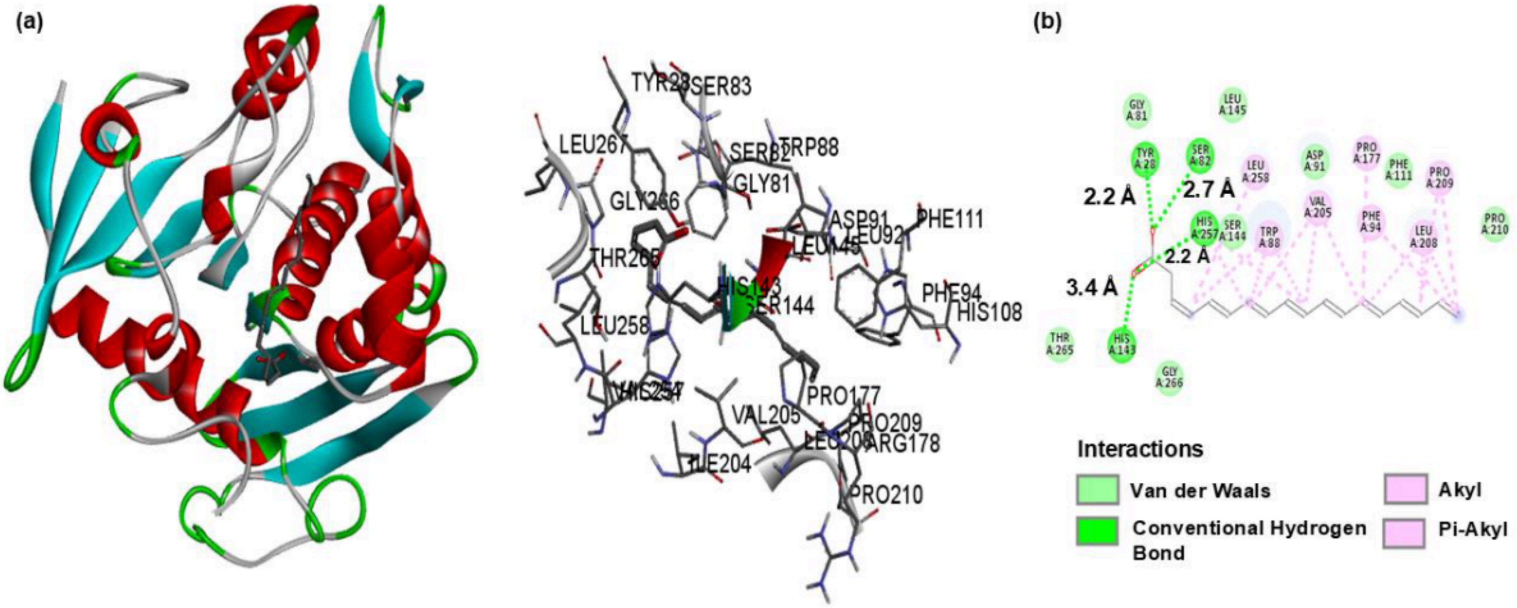

Figure 1 (a-b). Predicted binding conformations of stearic acid (C18) within the RML catalytic site, showing (a) three-dimensional ligand interactions (zoomed view) and (b) two-dimensional interaction diagram, generated using Discovery Studio

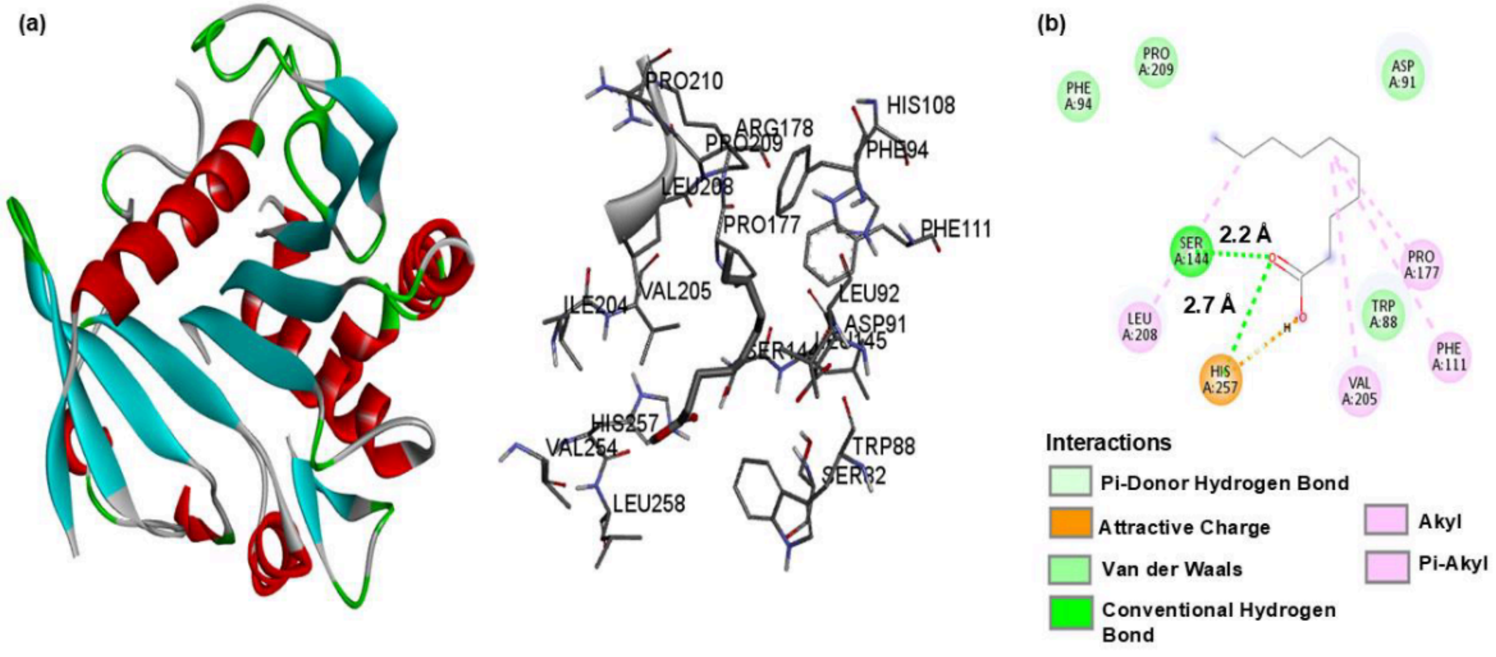

Figure 2 (a-b). Predicted binding conformations of decanoic acid (C10) within the RML catalytic site, showing (a) three-dimensional ligand interactions (zoomed view) and (b) two-dimensional interaction diagram, generated using Discovery Studio

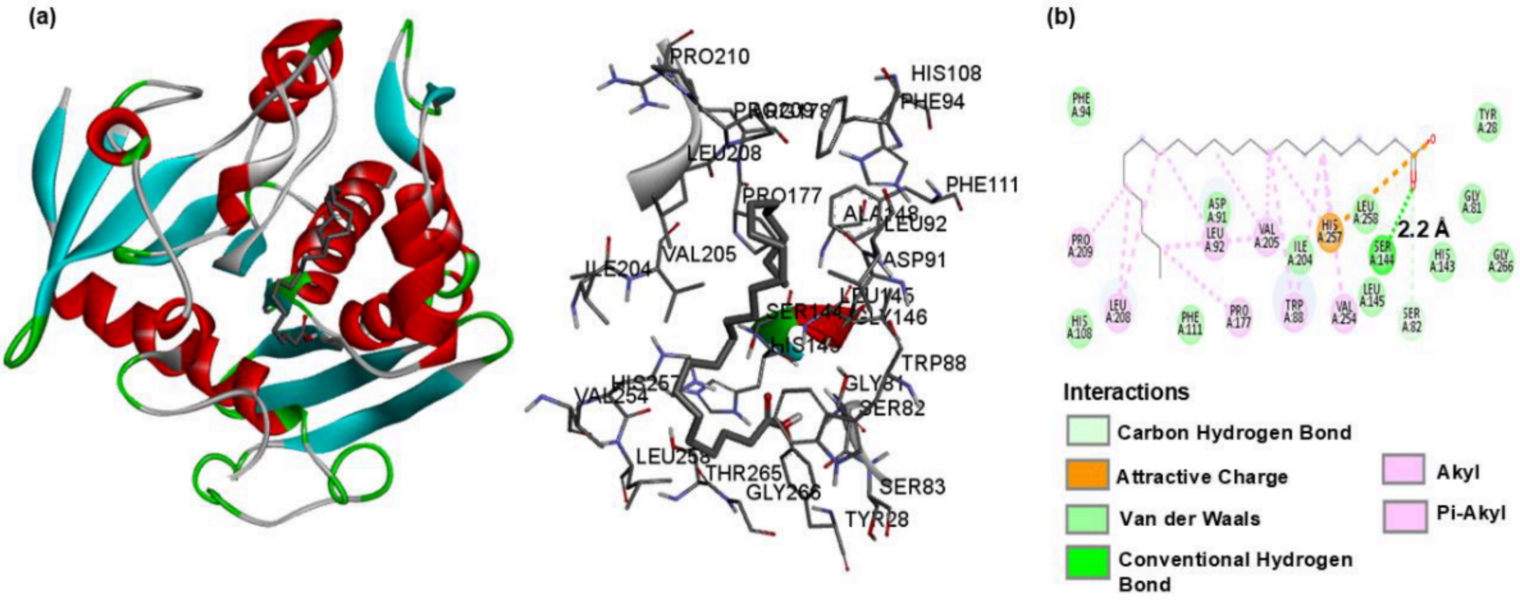

Figure 3 (a-b). Predicted binding conformations of docosanoic acid (C22) within the RML catalytic site, showing (a) three-dimensional ligand interactions (zoomed view) and (b) two-dimensional interaction diagram, generated using Discovery Studio

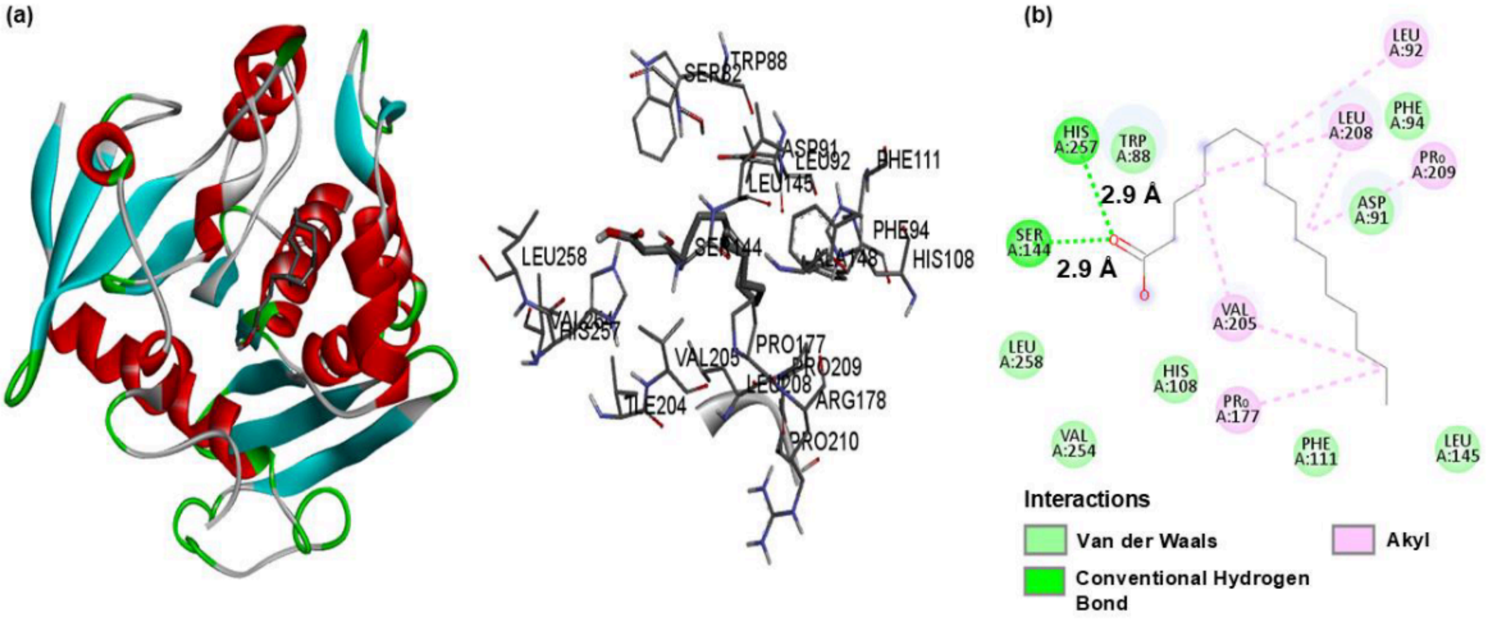

Figure 4 (a-b). Predicted binding conformations of palmitic acid (C16) within the RML catalytic site, showing (a) three-dimensional ligand interactions (zoomed view) and (b) two-dimensional interaction diagram, generated using Discovery Studio

Table 2 Summary of RML in NBR-1-ligand complexes docking analysis based on AutoDock Vina scores and discovery studio data

Complexes	Binding affinity (kcal/mole)	Van der Waals	Hydrogen bond	Hydrogen bond distance (Å)	Akyl and π-akyl	Attractive charge
RML-$C_{10}H_{20}O_2$ (decanoic acid, C10)	-4.9	Phe94, Pro209, Asp91, Trp88	Ser144 His257	2.2 2.7	Leu208, Pro177, Phe111, Val205	His257
RML-$C_{16}H_{32}O_2$ (palmitic acid, C16)	-5.5	Phe94, Asp91, Trp88, Leu258, Val254, His108, Phe111, Leu145	Ser144 His257	2.9 2.9	Pro209, Leu208, Pro177, Val205, Leu92	
RML - $C_{18}H_{36}O_2$ (stearic acid, C18)	-6.8	Thr265, Gly81, Leu145, Ser144, Gly266, Phe111, Asp91, Pro210	Tyr28 His257 Ser82 His143	2.2 2.2 2.7 3.4	Leu258, Trp88, Pro209, Leu208, Pro177, Val205, Phe94	
RML - $C_{22}H_{44}O_2$ (docosanoic acid, C22)	-6.1	Phe94, Tyr28, Gly81, Gly266, His143, Leu145, Leu258, Ile204, His108, Phe111, Asp91	Ser144	2.2	Leu92, Trp88, Pro209, Leu208, Pro177, Val205, Val254	His257

Carbon hydrogen bond was observed for RML-$C_{22}H_{44}O_2$ (docosanoic acid, C22) alone with Ser82.

The molecular docking results showed that the RML in NBR-1-lipid complexes had binding energies that ranged between -6.8 to -4.9 kcal/mole, with C18 having the lowest binding energy of -6.8 kcal/mole (Figure 1, Table 2). The lowest binding energy for C18 suggests higher stability level in the RML in NBR-1–C18 complex. In contrast, the RML in NBR-1-C10 complex demonstrated the highest binding energy (-4.9 kcal/mole) (Figure 2, Table 2), indicating the lower selectivity of RML in NBR-1 towards this short-chain fatty acid. These findings supported the indication made by Dong *et al*. [16] that RML prefers to form a more stable complex with 'the middle to long fatty acid side chains' than short-chain ones. As for the RML in NBR-1-C22 complexes (Figure 3, Table 2) and RML in NBR-1-C16 (Figure 4, Table 2), their binding energies correspondingly were -6.1 and -5.5 kcal/mole.

Following the recommended range for intermolecular hydrogen bonds (≤ 3.5Å) suggested by the previous researchers [34], the categorization of hydrogen bonds that formed between the RML in NBR-1 and the four ligands was made. It was observed that the RML in NBR-1-C18 complex exhibited the highest number of hydrogen bonds involving Tyr28, His257, Ser82, and His143, with bond distances of 2.2 Å, 2.7 Å, and 3.4 Å, respectively. In contrast, the RML in NBR-1-C10 and RML in NBR-1-C16 complexes only formed hydrogen bonds through Ser144 and His257. The hydrogen bond distances in the NBR-1-C10 complex were shorter, measuring 2.2 Å for Ser144 and 2.7 Å for His257, compared to the NBR-1-C16 complex, which showed distances of 2.9 Å for both residues. For the RML in NBR-1-C22 complex, hydrogen bonding involved only one residue, Ser144, with a distance of 2.2 Å.

In addition, the molecular docking results revealed the formation of van der Waals forces, alkyl and π-alkyl interactions, and carbon-hydrogen bonds with RML in NBR-1 residues. In general, the van der Waals forces occurred between residues, Gly81, Trp88, Asp91, His108, Phe111, His143, Ser144, Leu145, Ile204, Pro209, Pro210, Val254, Leu258, Thr265 and Gly266 (Figure 1-4). As for the alkyl and π-alkyl interactions, the RML in NBR-1 residues involved were Leu208, Pro177, Phe111, Val205, Leu208, Leu92, Leu258, Trp88, Pro209, Pro177, Phe94, Val254 (Figure 1-4, Table 2). In addition to the van der Waals forces observed with Thr265, Gly81, Leu145, Ser144, Gly266, Phe111, Asp91 and Pro210, RML in NBR-1-C18 also showed alkyl and π-alkyl interactions (Leu 258, Trp 88, Pro 209, Leu 208, Pro 177, Val 205, Phe 94) (Figure 1, Table 2). The RML in NBR-1-C10 complex specifically interacted by van der Waals forces with only four residues, namely Phe94, Pro209, Asp91, and Trp88, followed by alkyl and π-alkyl interactions with Leu208, Pro177, Phe111 and Val205 as well as the electrostatic interactions (attractive charge) (His257) (Figure. 2, Table 2).

While van der Waals forces with Phe94, Tyr28, Gly81, Gly266, His143, Leu145, Leu258, Ile204, His108, Phe111, Asp91 were observed for RML in NBR-1-C22 complex, the alkyl and π-alkyl interactions prevailed with Leu92, Trp88, Pro209, Leu208, Pro177, Val205, Val254 (Figure 3, Table 2). In addition to the electrostatic interactions (attractive charge) (His257), the carbon-hydrogen bond occurred with Ser-82 for NBR-1-C22 (Figure 3). As for RML in NBR-1-C16, van der Waals (Phe94, Asp91, Trp88, Leu258, Val254, His108, Phe111 and Leu145), as well as alkyl and π-alkyl interactions (Pro209, Leu208, Pro177, Val205 and Leu92), were also observed (Figure 4, Table 2). Therefore, based on the hydrogen bonds and their close distances between RML in NBR-1 and the four ligands, plus the formation of van der Waals forces, alkyl and π-alkyl interactions and carbon-hydrogen bond with RML in NBR-1 residues, it appears that the RML in NBR-1 is a useful biosensor for detecting fatty acids (C10, C16, C18 and C22) on latent fingermarks.

Molecular Dynamics (MD) Simulation of RML–ligand Complexes

To verify the findings of molecular docking, the complexes between RML in NBR-1 and the common lipid constituents in fingermarks were subjected to MD simulation. In order to examine the properties of the NBR-1–ligand complexes, five distinct analyses were conducted namely RMSD, RMSF, Rg, hydrogen bond and MMPBSA.

Root Mean Square Deviation (RMSD)

Conformational stability of the RML in NBR-1-ligand complexes was assessed using RMSD for tracking structural deviations [35], where stability corresponds to values near 1-3 Å (0.1-0.3 nm) [35]. Triplicate 100 ns MD simulations tested the computationally predicted interactions between RML in NBR-1 and the four fatty acids. Results, presented in Figure 5 (a-e), show the (a) combined average RMSD for RML in NBR-1 with all ligands and individual trajectories for (b) C10 (decanoic acid), (c) C16 (palmitic acid), (d) C18 (stearic acid), and (e) C22 (docosanoic acid). Equilibrium was achieved earliest by RML in NBR-1-C18 (~25 ns; 0.18 nm) and latest by RML in NBR-1-C16 (~80 ns; 0.24 nm). RML in NBR-1-C22 equilibrated at ~45 ns (0.20 nm), and RML in NBR-1-C10 at ~55 ns (0.23 nm). Notably, the RML in NBR-1-C18 complex exhibited the highest stability, evidenced by sustained low RMSD fluctuations (0.15-0.25 nm) throughout the simulation. This enhanced stability aligns with molecular docking results suggesting RML in NBR-1's preferential interaction with saturated long-chain fatty acids. Importantly, the NBR-1-C10 combination exhibited somewhat greater fluctuations (0.12−0.28 nm) when compared with the RML in NBR-1-C22 (0.12−0.25 nm) and RML in NBR-1-C16 (0.12−0.28 nm) complexes, prior to achieving the state of stability. Regarding the RML in NBR-1-C10, this complex is the most compact. As such, it can be construed that all RML in NBR-1-ligand complexes investigated here demonstrated relatively good stability with reasonable quality binding modes based on the estimated small range of RMSD fluctuation (0.10–0.28 nm). Therefore, while advocating that the RML in NBR-1 favoured the longer chain of fatty acids (C16-C22), its affinity towards the shorter ones (C10) also appears reasonably stable. This is particularly interesting since the findings of RMSD supported the use of RML-MWCNTs (NBR-1) as a biosensor for a wider range of fatty acids that may prevail on latent fingermarks.

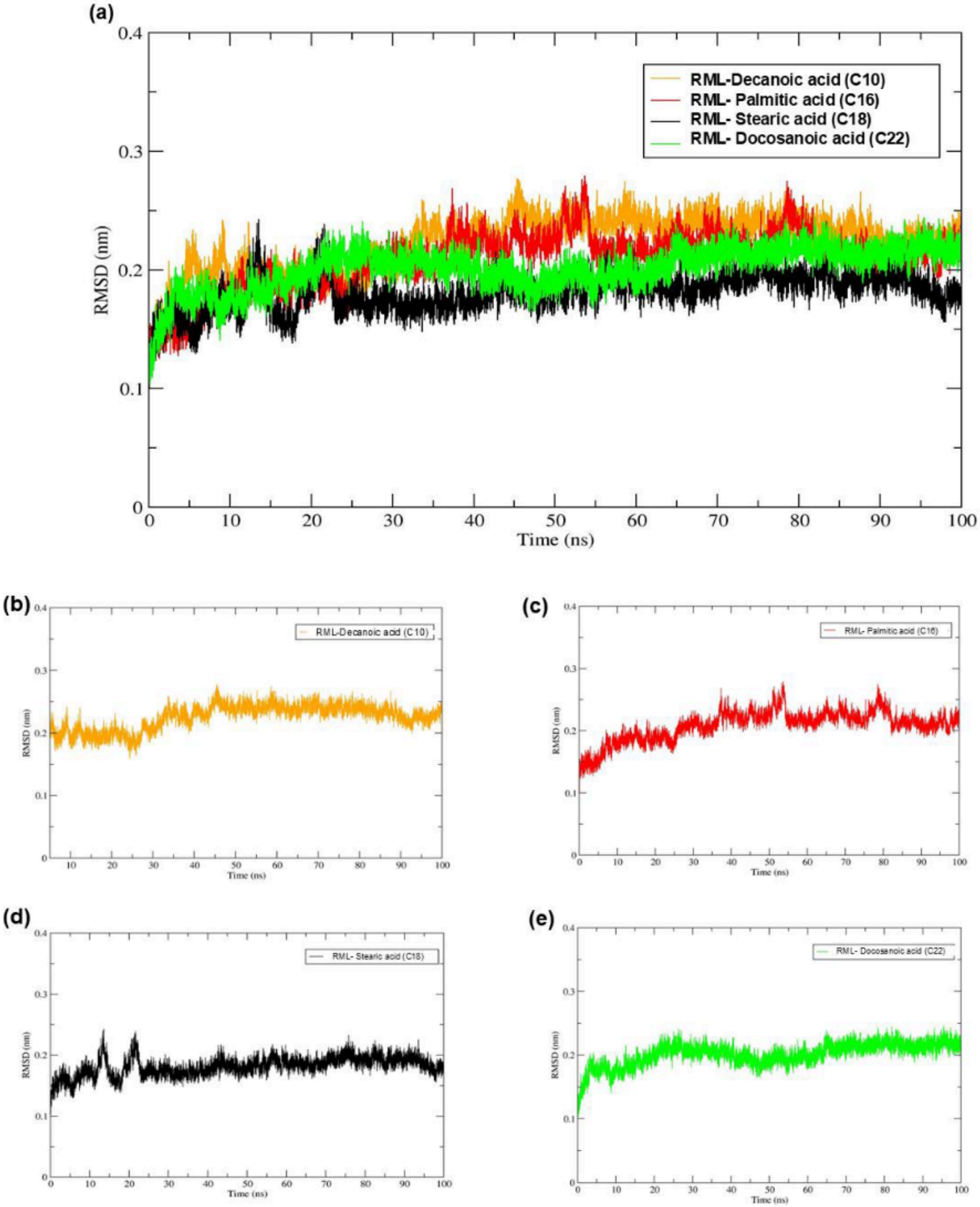

Figure 5 (a-e). The (a) overall average RMSD for the RML in NBR-1-four specific ligands: as well as the individual (b) decanoic acid (C10), (c) palmitic acid (C16), (d) stearic acid (C18), and (e) docosanoic acid (C22), obtained from MD simulations (100 ns)

Root Mean Square Fluctuation (RMSF)

Researchers [33, 35, 36] have suggested the use of RMSF in measuring the flexibility of an amino acid residue complexes with enzymes. In this context, a high RMSF value would signify greater flexibility in the complex, indicating increased movement during simulation. Conversely, a lower RMSF value suggests that the complex has achieved stability [37,38]. The (a) overall average RMSF for the RML in NBR-1-four specific ligands: as well as the individual (b) decanoic acid (C10), (c) palmitic acid (C16), (d) stearic acid (C18), and (e) docosanoic acid (C22), obtained from MD simulations (100 ns) are depicted in Figure 6 (a-e). Results revealed that all RML in NBR-1–ligand complexes exhibited stability, with little changes in RMSF values (ranging from 0.05 to 0.38 nm) (Figure. 6 (a-e)), with the RML in NBR-1-C18 being the most stable complex than other RML in NBR-1-complexes, exhibiting the least amount of fluctuation (0.04 to 0.30 nm). The residues linking the RML in NBR-1-C18 complex were Ile6 (0.32 nm), Gly163 (0.26 nm) and Thr269 (0.25 nm). Likewise, the second most stable complex was RML in NBR-1-C22 (0.04 to 0.31 nm), showing interactions with four residues, namely Ile6 (0.25 nm), Arg86 (0.24 nm), Pro250 (0.31 nm) and Thr269 (0.26 nm). As for the RML in NBR-1-10 complex, the interaction residues were of Ile6 (0.31 nm), Arg86 (0.27 nm), Phe94 (0.26 nm) and Gly163 (0.22 nm), making it the third most stable complex (0.05 and 0.32 nm) followed by the RML in NBR-1–C16 acid complex (0.05 to 0.38 nm) which interacted with Ile6 (0.36 nm), His42 (0.31 nm), Leu164 (0.25 nm), Leu255 (0.36 nm) and Thr269 (0.34 nm).

In general, the RMSF reaffirms that RML in NBR-1 formed stable complexes with long-chain fatty acids (less flexibility), in concurrence with the findings of RMSD and molecular docking. However, the RMSF also revealed that RML in NBR-1-C16 was the least stable, slightly different from the earlier molecular docking result that indicated the RML in NBR-1-C10 being the least stable one. In this context, previous researchers [22,33] cautioned that it is vital for the lipase–ligand complexes to have low RMSF values for the ligand binding sites to indicate their stability. The fact that the RMSF values for all complexes observed here were low (0.05 to 0.38 nm), it can be construed that all the complexes were stable, insinuating the suitability of RML in NBR-1 as a broader range biosensor for detecting varying fatty acids of wet latent fingermarks.

Radius of Gyration (Rg)

The Rg quantifies structural compactness within each complex throughout the MD simulation. A consistent Rg measurement signifies a rigid and stable protein-ligand interaction, whereas elevated Rg values denote complex instability [38]. Figure 7 (a-e) illustrates the (a) combined mean RMSF for RML in NBR-1 complexed with four specific ligands, alongside individual profiles for (b) decanoic acid (C10), (c) palmitic acid (C16), (d) stearic acid (C18), and (e) docosanoic acid (C22), derived from 100 ns MD simulations. Analysis revealed uniformly low Rg values with minimal fluctuation across all complexes. The RML in NBR-1-C18 complex attained steady-state conditions earliest, achieving equilibrium by 50 ns with a mean Rg of 1.70 nm. In contrast, the RML in NBR-1-C10 and NBR-1-C22 complexes stabilized later, reaching equilibrium at 70 ns and 72 ns, respectively, both exhibiting an average Rg of 1.71 nm. The NBR-1-C16 complex required 80 ns to equilibrate, yielding a mean Rg value of 1.73 nm. These Rg observations align with the RMSD (Figure 5a) and RMSF (Figure 6a) datasets, confirming the RML in NBR-1–C18 complex possesses the greatest structural rigid, while the RML in NBR-1–C16 complex is the least stable. The consistently low average Rg values (1.70-1.73 nm) observed for all RML in NBR-1-ligand complexes indicate robust stability, likely attributed to tight spatial proximity between the receptor's ligand-binding module (RML) and the ligands [21].

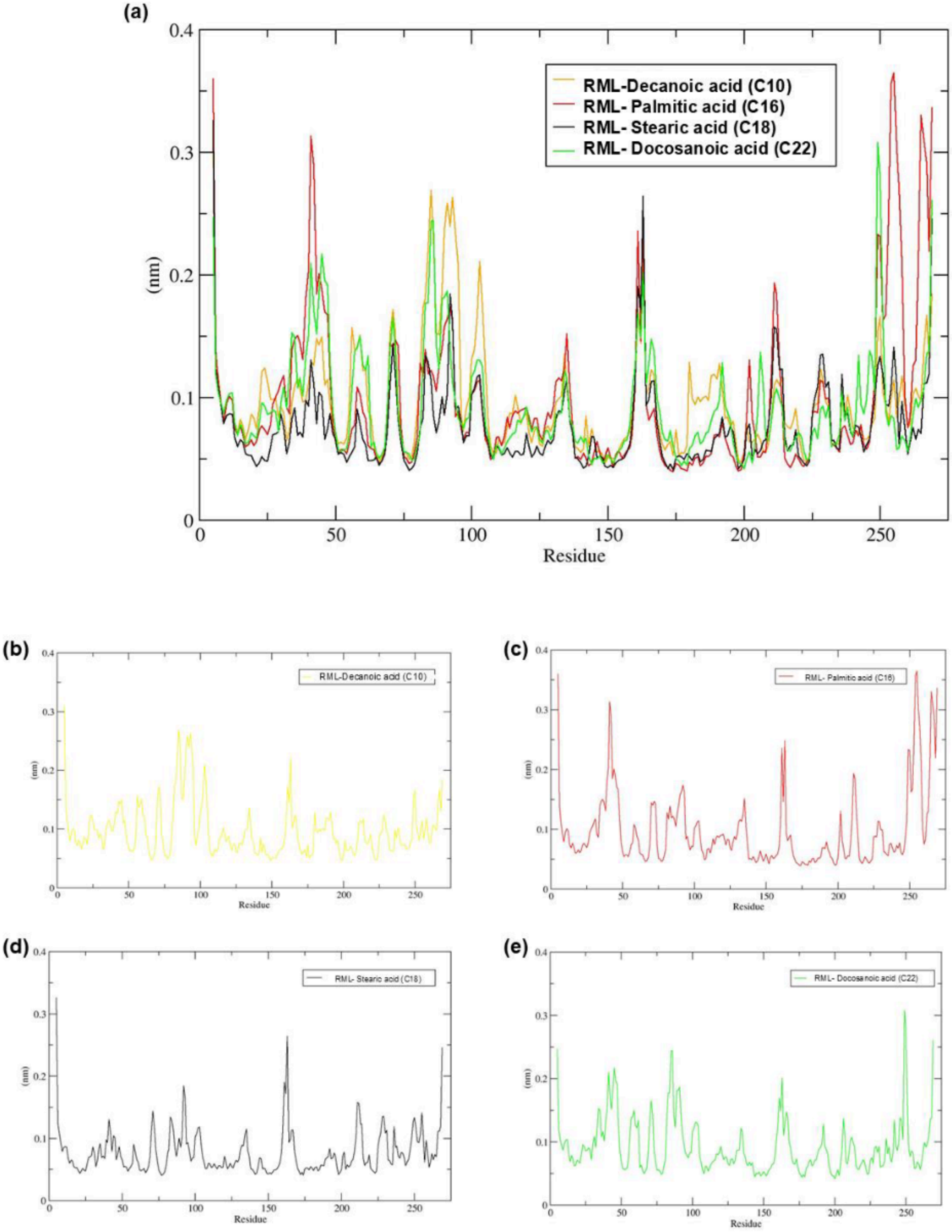

Figure 6 (a-e). The (a) overall average RMSF for the RML in NBR-1-four specific ligands: as well as the individual (b) decanoic acid (C10), (c) palmitic acid (C16), (d) stearic acid (C18), and (e) docosanoic acid (C22), obtained from MD simulations (100 ns)

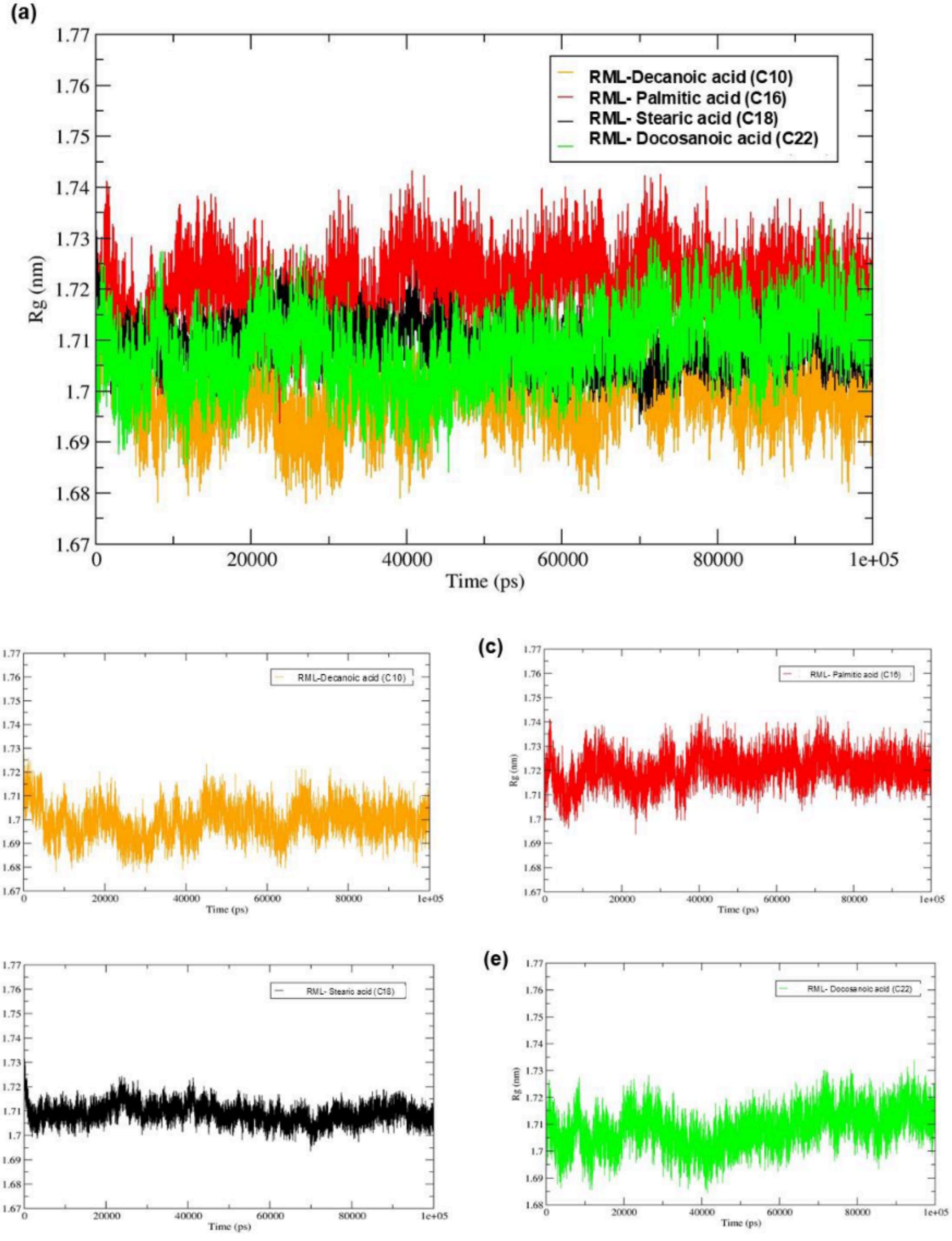

Figure 7 (a-e). The (a) overall average Rg for the RML in NBR-1-four specific ligands: as well as the individual (b) decanoic acid (C10), (c) palmitic acid (C16), (d) stearic acid (C18), and (e) docosanoic acid (C22), obtained from MD simulations (100 ns).

Hydrogen Bond

Previous researchers [40] have indicated that the overall hydrogen bond network interactions between the ligand and protein are important in warranting specificity (due to the accurate positioning of the ligand within the active site), as well as preserving a favorable conformation of the protein's active site.

Therefore, this present research examined the progression of hydrogen bond interactions with the corresponding ligands, as depicted in Figure 8 (a-e) and Table 2. The results demonstrated that the RML in NBR-1-C18 formed the maximum of four hydrogen bonds, stabilizing at 60 ns. This finding supported the notion that NBR-1-C18 exhibited both strong stability and flexibility. RML in NBR-1-C10 and RML in NBR-1-C16 formed two hydrogen bonds, whereas only one was formed for the RML in NBR-1-C22 complex. Therefore, the MD simulation results conveyed that the four protein-ligand complexes yielded structurally denser and stable state, which concurred with the molecular docking findings with distances between 2.2 to 3.4 Å, proving that the enzyme-ligand closely interacted over 100 ns.

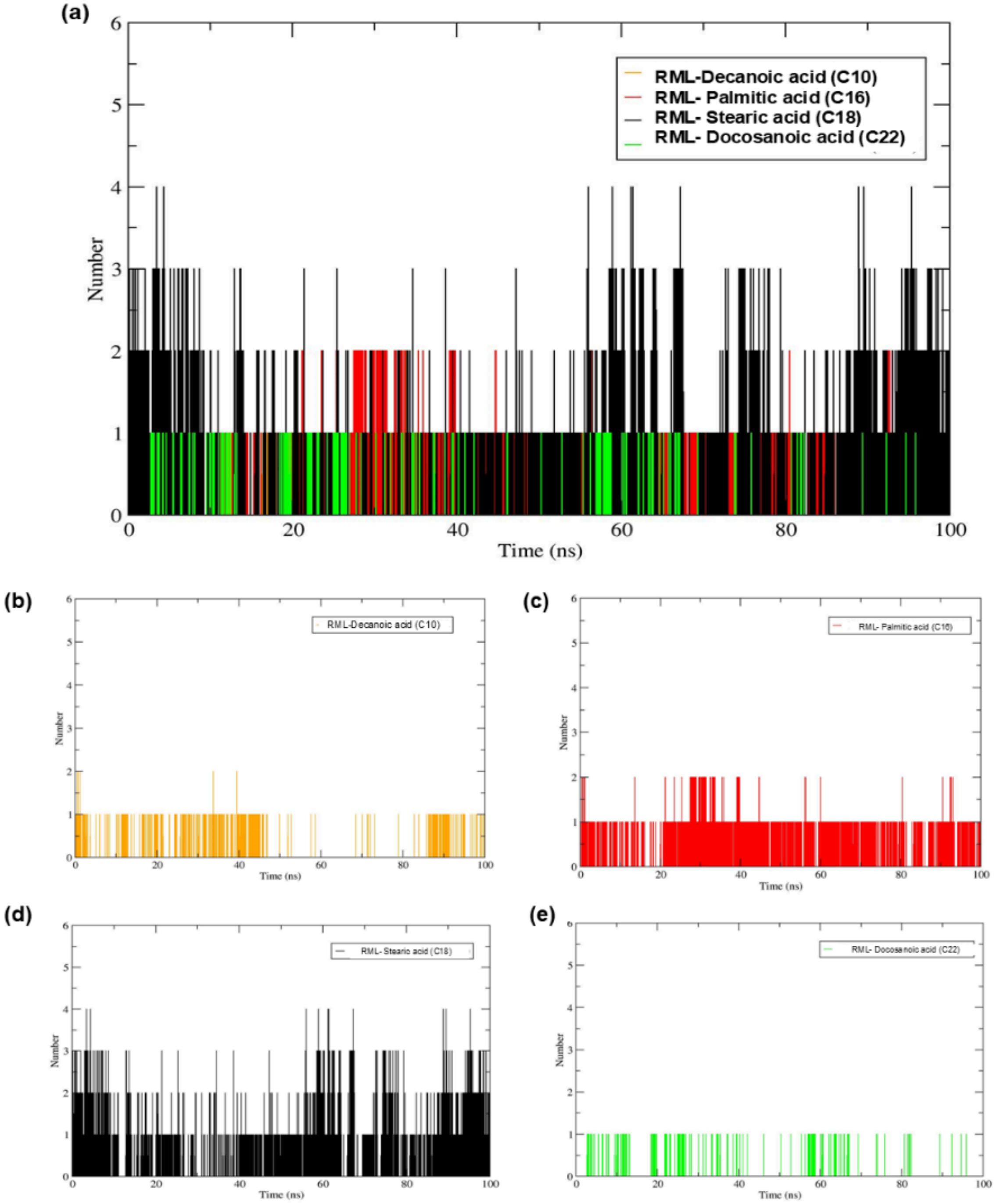

Figure 8 (a-e). The (a) overall average number of intermolecular hydrogen bond for the RML in NBR-1-four specific ligands: as well as the individual (b) decanoic acid (C10), (c) palmitic acid (C16), (d) stearic acid (C18), and (e) docosanoic acid (C22), obtained from MD simulations (100 ns)

MM-PBSA Binding Free Energy Calculation

Table 3 presents the binding free energies (kcal/mol) computed for the four specific RML in NBR-1-ligand complexes using MM-PBSA. Prior research indicates that the average binding free energy provides significant insight into enzyme-ligand interaction dynamics [30]. For the RML in NBR-1 complexes with decanoic acid (C10), palmitic acid (C16), stearic acid (C18), and docosanoic acid (C22), the binding free energy trajectories were computed directly from the final 100 ns of MD simulations via MM-PBSA. This analysis focused on pertinent energy components: van der Waals forces, electrostatic interactions, polar solvation, and non-polar solvation energies [29]. Andrusier *et al*. demonstrated that energy calculations derived from MD trajectories exhibit enhanced sensitivity and adaptability when the protein-ligand complex achieves sufficient conformational sampling throughout the production simulation phase [39]. Empirically, a greater number of hydrogen bonds between the ligand and residues critical for protein function often correlates with stronger binding affinity, reflected by more negative binding free energy values [35].

Data presented in Table 3 confirm that MM-PBSA calculations validate the MD simulation outcomes. Strong binding affinity for the RML in NBR-1-C18 complex is evidenced by its computed binding free energy of -173.783 ± 8.660 kcal/mol. Similarly, RML in NBR-1-C22 exhibited a binding free energy of -155.596 ± 15.064 kcal/mol, while RML in NBR-1-C10 yielded -111.564 ± 10.750 kcal/mol. In contrast, RML in NBR-1-C16 showed a substantially reduced affinity with a binding free energy of -81.465 ± 8.452 kcal/mol. This MM-PBSA analysis corroborates RML in NBR-1-C18 as the most stable complex, aligning with stability metrics derived from RMSD, RMSF, and Rg analyses. Collectively, the computational evidence detailing interactive residues, binding energetics, and mechanistic insights would substantiate RML in NBR-1's potential as a candidate reagent for visualizing latent fingermarks on wet non-porous substrates. Consequently, empirical validation through laboratory assessment of RML in NBR-1-treated fingermarks becomes warranted.

Table 3 Binding free energies from MM-PBSA in kcal/mol for the RML in NBR-1-four specific ligands: decanoic acid (C10), palmitic acid (C16), stearic acid (C18), and docosanoic acid (C22), obtained from MD simulations

Complexes	**Energy components (kJ/mol)**				
	ΔE_{vdW}	**ΔE_{ele}**	**ΔG_{polar}**	**$\Delta G_{nonpolar}$**	**$\Delta G_{binding}$**
RML-$C_{10}H_{20}O_2$ (decanoic acid)	-146.73±13.98	-2.88±2.54	55.57±9.08	-17.52±1.32	-111.56±10.75
RML-$C_{16}H_{32}O_2$ (palmitic acid)	-109.66±9.11	-46.87±7.30	87.86±5.54	-12.80±0.70	-81.47±8.45
RML-$C_{18}H_{36}O_2$ (stearic acid)	-196.99±6.23	-7.43±3.52	53.27±9.25	-22.62±0.81	-173.78±8.66
RML-$C_{22}H_{44}O_2$ (docosanoic acid)	-219.40±15.51	-15.03±10.81	101.85±18.51	-23.02±1.69	-155.60±15.06

Characterization of Synthesized NBR-1

Attenuated Total Reflectance – Fourier Transform Infrared Spectroscopy (ATR-FTIR)

ATR-FTIR spectra for F-MWCNTs and RML-MWCNTs are presented in Figure 9a and 9b, respectively. The broad absorption band at 3308 cm⁻¹ (Figure 9a) is indicative of O-H stretching, consistent with hydroxyl groups from adsorbed atmospheric moisture and oxidative surface modifications introduced during MWCNT purification [41,42]. Acid functionalization using concentrated HNO_3:H_2SO_4 (1:3) generated characteristic bands at 1640 cm⁻¹ (C=O stretching) and 3308 cm⁻¹ (O-H stretching), signifying carboxylic acid group formation. Current interpretations attribute the 1640 cm⁻¹ band to carbonyl stretching within benzoic acid derivatives attached to MWCNT sidewalls or tube termini [13]. Additionally, moderate-intensity bands at 1256 cm^{-1} correspond to C-O vibrations of surface carboxylate moieties in F-MWCNTs (Figure 9a). Successful RML immobilization onto F-MWCNTs (forming NBR-1) was confirmed by a distinct spectral shift: the amide C=O stretching frequency migrated from 1640 cm^{-1} (F-MWCNTs) to 1653 cm^{-1} (RML-MWCNTs). Further evidence of RML adsorption manifests as reduced intensity and broadening of carboxylate C-O vibrational peaks (1256 cm^{-1}) in RML-MWCNTs (NBR-1) relative to F-MWCNTs (Figure 9b), confirming polypeptide chain presence. Structural analysis indicates a short polypeptide segment (termed a lid or flap) adopts a closed conformation shielding the enzyme's active core from solvent exposure [44].

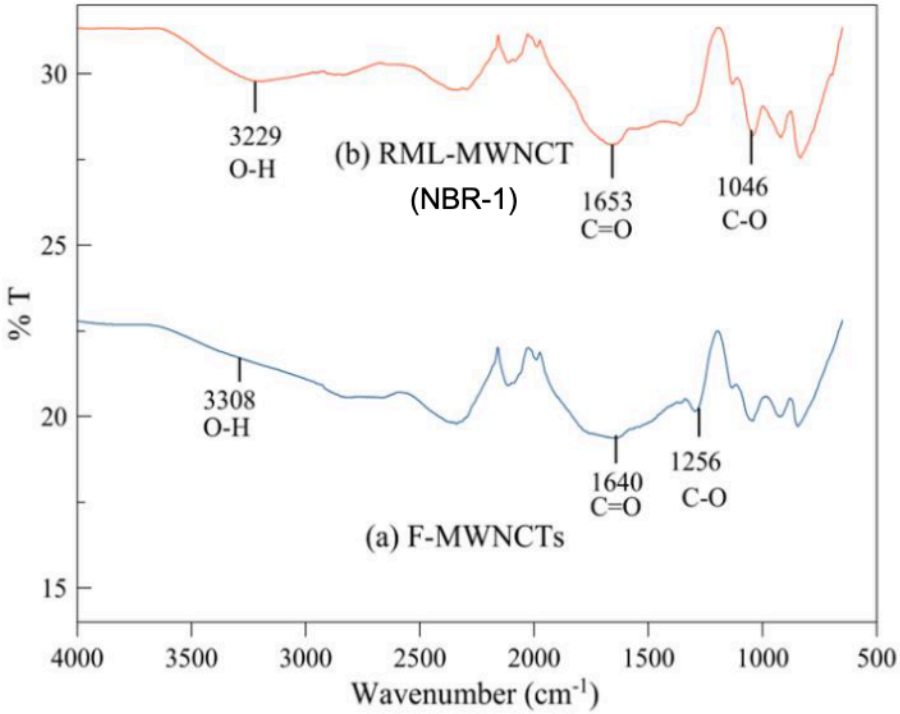

Figure 9 (a-b). ATR-FTIR spectral profiles for (a) F-MWCNTs and (b) RML-MWCNTs (designated as NBR-1)

Field Emission Scanning Electron Microscopy (FESEM)

Figure 10 (a) and 10 (b) illustrate the respective morphological features of F-MWCNTs and RML-MWCNTs (NBR-1). Following RML immobilization onto F-MWCNTs, the nanotube diameter range increased to 29.8–35.8 nm from an initial 13.9–16.0 nm. This finding provides definitive evidence for successful RML molecule attachment to the F-MWCNT surface, aligning with prior investigations utilizing functionalized MWCNTs as nanosupports for RML immobilization [42]. Furthermore, the observed surface roughening and increased thickness of RML-MWCNTs (NBR-1) likely arise from a uniform enzyme coating, consistent with earlier reports [44]. These morphological alterations collectively confirm effective RML immobilization onto the F-MWCNT substrate.

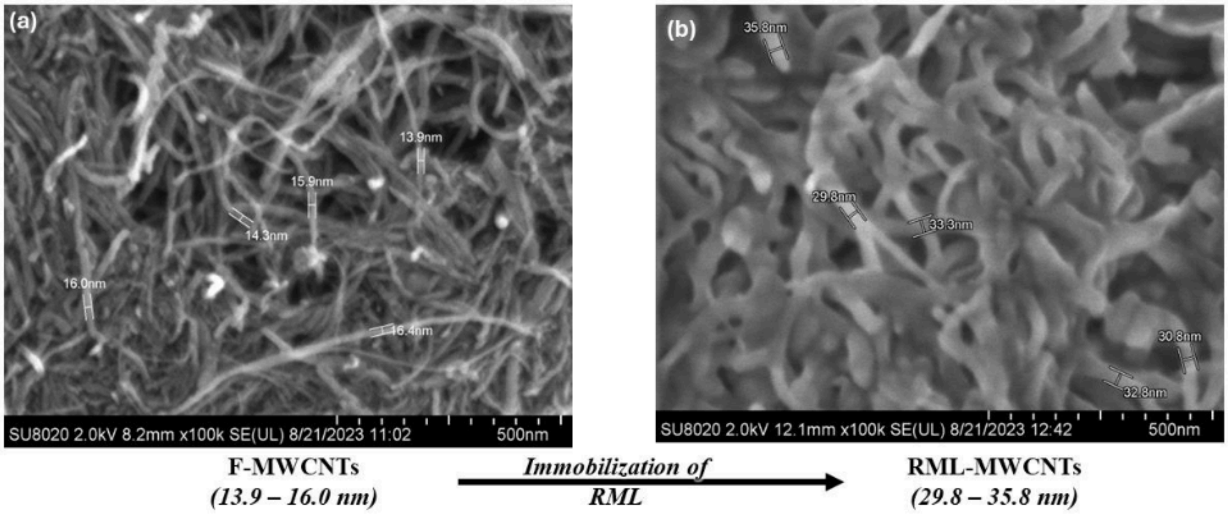

Figure 10 (a-b) FESEM microstructural features of (a) F-MWCNTs and (b) RML-MWCNTs (designated as NBR-1) deposited on a fingermark (100,000× magnification)

Additionally, the observed increase in the RML thickness might be attributed to its inclination to create biomolecular clusters on modified surfaces [44]. An example of the successful visualization of the latent fingermark using the NBR-1 is presented in Figure 11. The NBR-1 in the FESEM micrograph (Figure 11) clearly shows ridge patterns (outlined in red), which are useful for forensic identification. The exclusive localization of NBR-1 on the ridges of the fingermark, with only minimum impact on the surrounding region, suggests that NBR-1 selectively interacts with the lipid components of the fingermark, as seen in Figure 11.

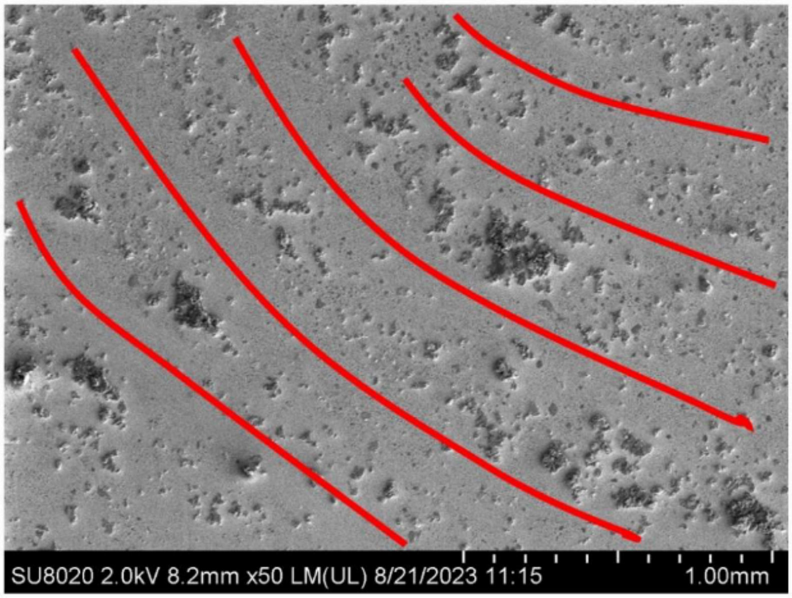

Figure 11. Photomicrograph (50x magnification) to show the ridges (outlined in red) of a visualized fingermark using NBR-1 under scanning electron microscope

Laboratory Assessment of NBR-1 for Visualizing Latent Fingermarks on Glass Slides Immersed in Laboratory-Controlled Tap Water

Physicochemical Parameters of the Water

This study evaluated the novel NBR-1 reagent's efficacy for latent fingermark visualization under controlled laboratory conditions. Glass substrates bearing fingermarks were fully immersed in tap water, with physicochemical parameters (pH, temperature, turbidity, dissolved oxygen) monitored daily over a 14-day period to standardize the discussion on environmental variables. It is pertinent to indicate here that no measures to control the physicochemical parameters of the water were attempted; the reported data were of the original conditions observed over the period of two weeks of immersions. These parameters were recorded to enable standardization of discussion, should other researchers attempt to replicate the experiment, and the physicochemical parameters of the water remain similar. Nonetheless, it is anticipated that substantial variations in these parameters would somehow affect the quality of visualized fingermarks.

Water pH remained consistently neutral to slightly alkaline (range: 7.27–7.81; mean ± SD: 7.54 ± 0.14), notably aligning with RML's optimal activity range (pH 7–8) [43]. This pH stability suggests favorable conditions for NBR-1-mediated fingermark development on submerged substrates. These physicochemical parameters exhibited minimal fluctuation: temperature (26.7–28.8°C; 27.81 ± 0.63), turbidity (0.04–0.26 NTU; 0.12 ± 0.06), and dissolved oxygen (7.15–7.92 mg/L; 7.74 ± 0.20). All values conformed to Malaysia's Class 1 water quality standards [46]. The observed inverse relationship between dissolved oxygen and temperature, attributable to reduced gas solubility in warmer water [45], manifested subtly here, consistent with restricted microbial activity [48,49] and negligible turbidity variation. Cumulatively, these findings demonstrate insignificant deviations in the water's physicochemical properties throughout the experimental timeframe.

Laboratory-controlled Assessment of NBR-1

Figure 12 (a) and (b) depict the representative visualized latent groomed fingermarks on glass slides immersed in water for 14 consecutive days using the newly synthesized NBR-1 and the commercially available SPR, respectively. Results revealed that the visualized groomed fingermark was considerably enhanced by the NBR-1 (average m-CAST absolute scale: 4) than that of the SPR (average m-CAST absolute scale: 2). Furthermore, it can be clearly seen that the groomed fingermark visualized by NBR-1 had lesser amount of background interference and much clearer than the one developed by SPR, consistent with the previous research that utilized a different lipase conjugate (CRL-MWCNTs) reported by previous researchers [4]. The findings corroborate the fact that enzymes like RML (in NBR-1) and CRL (in NBR) are particular and selective for their lipid substrates [49]. While faint visualization was achieved with RML alone, improved contrast and higher quality of latent groomed fingermarks were obtained when RML immobilized onto FMWCNTs (NBR-1) was utilized, whereby F-MWCNTs acted as the contrasting agent. As such, this observation pertained to the specificity of lipases, such as RML, reacting with lipids on groomed fingermarks. In contrast, specific substrates for SPR have not been explicitly documented [14]. Since the mode of interaction for SPR to visualize latent fingermarks on wet, non-porous objects is still unknown [8], the appropriate discussion regarding its preference for the non-water-soluble constituents of fingermarks cannot be fully offered.

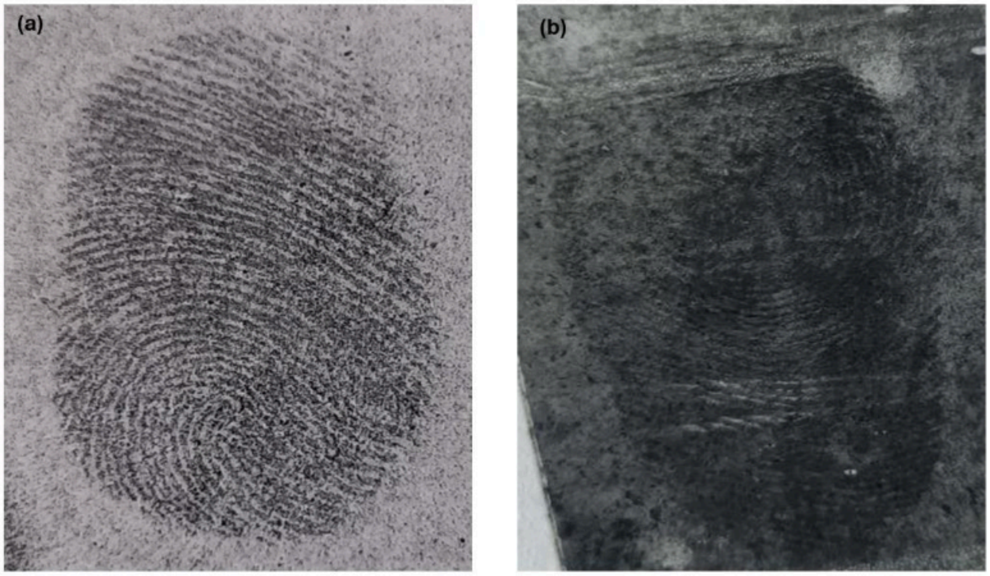

NBR1 (RML-MWCNTs)

m-CAST scale: 4

SPR

m-CAST scale: 2

Figure 12. Representative photographs of the visualized latent fingermarks on glass slides immersed for 14 consecutive days using (a) NBR-1 (RML-MWCNTs) and (b) SPR

Table 4 represents the quality of visualized groomed fingermarks (m-CAST scale) on glass slides immersed for 7 and 14 days in water under laboratory-controlled conditions for male and female participants using the newly synthesized NBR-1. In general, the female participant exhibited significantly superior fingermark quality ($p < 0.05$) compared to the male participant. Moreover, statistically, a better quality of fingermarks was observed for the female participant on glass slides immersed for 7 days compared to those visualized after 14 days of immersion ($p < 0.05$). However, no significant difference was evident over the two periods of immersion (7 and 14 days) for fingermarks from the male participant ($p > 0.05$).

Table 4 Visual quality assessment (m-CAST scale) of fingermarks developed using novel NBR-1 on laboratory-submerged glass slides under controlled conditions

Gender	**Durations of exposure**	
	Day 7	**Day 14**
Female	$3.0 \pm 1.0^{a,b}$ (2-4)	2.0 ± 0 (2-2)
Male	1.5 ± 0.6 (1-2)	1.0 ± 0 (1-1)

The data are presented as mean ± standard deviation with ten replicates for each duration and gender. The quality of the fingermarks was verified by two individuals. Comparisons of the quality between the two intervals as well as gender were performed using the Independent Sample t-test with a level of significance of 0.05. The quality of fingermarks was significantly better ($p < 0.05$) for the female subject than that of male (^{a}). While statistically better quality of fingermarks in female ($p < 0.05$) was observed on day-7 (^{b}) when compared with that of day-14, no significant difference was evident for the same in male.

Moreover, in concurrence to the findings reported by previous researchers that studied on the quality of the visualized fingermarks over an extended duration of water immersion [3,50,51,52], a noticeable decline in the quality of fingermarks over time was also observed in all samples here, following their visualization using NBR-1. Such a phenomenon can be attributed to the hydrolysis of lipid by microbes, apart from the destruction of fingermark residues *via* water mechanical effect [8].

Conclusions

This study establishes the novel NBR-1 (based on RML immobilized on f-MWCNTs) as a highly effective reagent for visualizing latent fingermarks on forensically challenging wet substrates. These findings support the integration of NBR-1 into standard forensic protocols for underwater crime scene evidence. This research makes a unique contribution by demonstrating, through an integrated bioinformatics and experimental approach, that RML's specific affinity for a broad spectrum of fatty acid residues (C10–C22) enables clear fingermark development on surfaces submerged in water for up to two weeks. This specificity ensures high-contrast visualization with minimal background interference. Therefore, the NBR-1 is a robust, green nanobio-based solution for wet evidence, bridging a critical gap in current fingermarks visualization techniques. Future work shall focus on validating this method under a wider range of operational environmental conditions, as suggested by the International Fingerprint Research Group guideline [22].

Limitations

One limitation for this present research was the fact that only two donors (one male and one female) were included, hence limiting generalizability of the findings. Having said that, it is pertinent to mention here that the aim of this research was on the feasibility aspect of utilizing RML nano-conjugate, for the first time, in visualizing latent fingermark on wet objects. This was in line with the prescribed Phase 1 guideline of the International Fingerprint Research Group [22]. Considering the positive findings reported here, the involvement of larger sample size would be required during the following optimization, sensitivity and specificity assays, as well as field work assessments [22], complying with the subsequent phases of the prescribed guideline by International Fingerprint Research Group, focusing on the natural fingermarks.

Conflicts of Interest

The authors declare that there is no conflict of interest regarding the publication of this paper.

Acknowledgment

This research project was supported by the Ministry of Higher Education Malaysia Fundamental Research Grant Scheme, FRGS/1/2023/STG01/UTM/02/1 and Universiti Teknologi Malaysia Fundamental Research Grant, Q.J130000.3854.22H68.

References

[1] Swanson, C. M. R. C., Chamelin, N. C., Territo, L., & Taylor, R. W. (2019). *Criminal investigation* (12th ed.). McGraw-Hill Education.

[2] De Alcaraz-Fossoul, J., Zapico, S. C., Dean, E. R., Mueller, K. E., Johnson, C., & Roberts, K. A. (2021). Evaluation of latent fingermark color contrast as aging parameter under different environmental conditions: A preliminary study. *Journal of Forensic Sciences, 66*(2), 719–736.

[3] Azman, A. R., Zulkifli, N. S., Mahat, N. A., Ahmad, W. A., Hamzah, H. H., & Abdul Wahab, R. (2019). Visualisation of latent fingerprints on non-porous object immersed in stagnant tap water using safranin-tinted *Candida rugosa* lipase reagent. *Malaysian Journal of Fundamental and Applied Sciences, 15*(6), 781–783. https://doi.org/10.11113/mjfas.v15n6.1416.

[4] Azman, A. R., Mahat, N. A., Abdul Wahab, R., Ahmad, W. A., & Ismail, D. (2022). Preliminary forensic assessment of the visualised fingerprints on nonporous substrates immersed in water using the green and optimised novel nanobio-based reagent. *Scientific Reports, 12*(1). https://doi.org/10.1038/s41598-022-18929-8.

[5] Ting, C. W., Mahat, N. A., Azman, A. R., Muda, N. W., & Anuar, N. (2021). Performance of the nanobio-based reagent for visualising wet fingerprints exposed to different levels of water salinity. *Journal of Clinical and Health Sciences, 6*(1, Special), 32–43. https://doi.org/10.24191/jchs.v6i1.

[6] Woodcock, L., Gooch, J., Wolff, K., Daniel, B., & Frascione, N. (2023). Fingermarks in wildlife forensics: A review. *Forensic Science International*, 111781. https://doi.org/10.1016/j.forsciint.2023.111781.

[7] Schönfeld, P., & Wojtczak, L. (2016). Short- and medium-chain fatty acids in energy metabolism: The cellular perspective. *Journal of Lipid Research, 57*, 943–954. https://doi.org/10.1194/jlr.R067629.

[8] Azman, A. R., Mahat, N. A., Abdul Wahab, R., Ahmad, W. A., Huri, M. A. M., & Hamzah, H. H. (2019). Relevant visualization technologies for latent fingerprints on wet objects and its challenges: A review. *Egyptian Journal of Forensic Sciences, 9*(1), 1–13. https://doi.org/10.1186/s41935-019-0129-3.

[9] Sørli, J. B., *et al.* (2023). Pulmonary toxicity of molybdenum disulphide after inhalation in mice. *Toxicology, 485*, 153428. https://doi.org/10.1016/j.tox.2023.153428.

[10] Zou, W., *et al.* (2024). MoS_2 nanosheets at low doses induced cardiotoxicity in developing zebrafish via ferroptosis: Influence of lateral size and surface modification. *Environmental Science & Technology*. https://doi.org/10.1021/acs.est.4c08685.

[11] Gopalakrishnan, T., *et al.* (2023). Effects of molybdenum disulfide nano-particles' concentration on waste cooking oil nanofluid in reduction feed force in CNC wet machining of SAE 1144 steel. *Materials Today: Proceedings*. https://doi.org/10.1016/j.matpr.2023.03.442.

[12] Xu, Z., *et al.* (2023). The ecotoxicity of single-layer molybdenum disulfide nanosheets on freshwater microalgae *Selenastrum capricornutum*. *Process Safety and Environmental Protection, 175*, 426–436. https://doi.org/10.1016/j.psep.2023.05.073.

[13] Srivastava, S., *et al.* (2019). Safety assessment of the pharmacological excipient, diethylene glycol monoethyl ether (DEGEE), using in vitro and in vivo systems. *DARU Journal of Pharmaceutical Sciences, 27*, 219–231. https://doi.org/10.1007/s40199-019-00264-5.

[14] Azman, A. R., *et al.* (2020). Characterisation and computational analysis of a novel lipase nanobio-based reagent for visualising latent fingerprints on water-immersed glass slides. *Process Biochemistry, 96*, 102–112. https://doi.org/10.1016/j.procbio.2020.05.033.

[15] Verma, L. M., Rao, N. M., Tsuzuki, T., Barrow, C. J., & Puri, M. (2019). Suitability of recombinant lipase immobilised on functionalised magnetic nanoparticles for fish oil hydrolysis. *Catalysts, 9*(5), 420. https://doi.org/10.3390/catal9050420.

[16] Dong, Z., Olofsson, K., Linares-Pastén, J. A., & Nordberg Karlsson, E. (2022). Investigation of structural features of two related lipases and the impact on fatty acid specificity in vegetable fats. *International Journal of Molecular Sciences, 23*(13), 7072. https://doi.org/10.3390/ijms23137072.

[17] Razi, N. I. M. N., Mahat, N. A., Abdul Wahab, R., Aida, R. A., Alwi, A. R., & Nordin, N. (2024). Microbial lipases as potential candidates for greener fingermark visualization technologies on wet non-porous objects: A review. *Malaysian Journal of Analytical Sciences, 28*(5), 1184–1209.

[18] Sufyan, M., *et al.* (2021). Identifying key genes and screening therapeutic agents associated with diabetes mellitus and HCV-related hepatocellular carcinoma by bioinformatics analysis. *Saudi Journal of Biological Sciences, 28*(10), 5518–5525. https://doi.org/10.1016/j.sjbs.2021.07.068.

[19] Mitra, D., *et al.* (2022). Evolution of bioinformatics and its impact on modern bio-science in the twenty-first century: Special attention to pharmacology, plant science and drug discovery. *Computational Toxicology, 24*, 100248. https://doi.org/10.1016/j.comtox.2022.100248.

[20] Tap, F. M., Zakaria, N. H., Majid, F. A. A., AKM, M. H., & Jamal, J. A. (2022). Repurposing mitragynine as anti-SARS-CoV-2 agent evidenced by in silico predictive approach. *Malaysian Journal of Fundamental and Applied Sciences, 18*(6), 644–653. https://doi.org/10.11113/mjfas.v18n6.2637.

[21] Lin, K. T., Mahat, N. A., Azman, A. R., Abdul Wahab, R., Oyewusi, H. A., & Abdul Hamid, A. A. (2023). Interaction of the nanobio-based reagent with sodium fluorescein and lipids via bioinformatics for forensic fingerprint visualisations. *Journal of Biomolecular Structure and Dynamics*, 1–8. https://doi.org/10.1080/07391102.2023.2186709.

[22] International Fingerprint Research Group. (2014). Guidelines for the assessment of fingermark detection techniques. *Journal of Forensic Identification, 64*(2), 174–200.

[23] O'Boyle, N. M., Banck, M., James, C. A., Morley, C., Vandermeersch, T., & Hutchison, G. R. (2011). Open Babel: An open chemical toolbox. *Journal of Cheminformatics, 3*, 1–14. https://doi.org/10.1186/1758-2946-3-33.

[24] Morris, G. M., *et al.* (2009). AutoDock4 and AutoDockTools4: Automated docking with selective receptor flexibility. *Journal of Computational Chemistry, 30*(16), 2785–2791. https://doi.org/10.1002/jcc.21256.

[25] Trott, O., & Olson, A. J. (2010). AutoDock Vina: Improving the speed and accuracy of docking with a new scoring function, efficient optimization, and multithreading. *Journal of Computational Chemistry, 31*(2), 455–461. https://doi.org/10.1002/jcc.21334.

[26] Peng, B., *et al.* (2020). Enzymatic synthesis of 1,3-oleic-2-medium chain triacylglycerols and strategy of controlling acyl migration: Insights from experiment and molecular dynamics simulation. *International Journal of Food Properties, 23*(1), 1082–1096. https://doi.org/10.1080/10942912.2020.1775645.

[27] Sraphet, S., & Javadi, B. (2025). Deciphering the structural complexity of esterases in *Amycolatopsis eburnea*: A comprehensive exploration of solvent accessibility patterns. *Computers in Biology and Medicine, 192*, 110361. https://doi.org/10.1016/j.compbiomed.2025.110361.

[28] Dassault Systèmes BIOVIA. (n.d.). *Discovery Studio Modeling Environment.*

[29] Kumari, R., Kumar, R., O. S. D. D. Consortium, & Lynn, A. (2014). g_mmpbsa – A GROMACS tool for high-throughput MM-PBSA calculations. *Journal of Chemical Information and Modeling, 54*(7), 1951–1962. https://doi.org/10.1021/ci500020m.

[30] Oyewusi, H. A., Huyop, F., Wahab, R. A., & Abdul Hamid, A. A. (2021). In silico assessment of dehalogenase from *Bacillus thuringiensis* H2 in relation to its salinity-stability and pollutants degradation. *Journal of Biomolecular Structure and Dynamics, 40*(19), 9332–9346. https://doi.org/10.1080/07391102.2021.1927846.

[31] Rajan, R., Zakaria, Y., Shamsuddin, S., & Nik Hassan, N. F. (2019). Fluorescent variant of silica nanoparticle powder synthesised from rice husk for latent fingerprint development. *Egyptian Journal of Forensic Sciences, 9*(1), 50. https://doi.org/10.1186/s41935-019-0155-1.

[32] Bandey, H. L., & Gibson, A. P. (2006). *Fingerprint development and imaging newsletter: Special edition*. Home Office Scientific Development Branch Investigative Enforcement Protection Section.

[33] Oyewusi, H. A., Huyop, F., & Wahab, R. A. (2020). Molecular docking and molecular dynamics simulation of *Bacillus thuringiensis* dehalogenase against haloacids, haloacetates and chlorpyrifos. *Journal of Biomolecular Structure and Dynamics, 40*(5), 1979–1994. https://doi.org/10.1080/07391102.2020.1835727.

[34] Oyewusi, H. A., Wu, Y.-S., Safi, S. Z., Wahab, R. A., Hatta, M. H. M., & Batumalaie, K. (2022). Molecular dynamics simulations reveal the inhibitory mechanism of Withanolide A against α-glucosidase and α-amylase. *Journal of Biomolecular Structure and Dynamics, 41*(13), 6203–6218. https://doi.org/10.1080/07391102.2022.2104375.

[35] Tran, Q.-H., *et al.* (2022). Structure-based 3D-pharmacophore modeling to discover novel interleukin 6 inhibitors: In silico screening, molecular dynamics simulations and binding free energy calculations. *PLoS One, 17*(4), e0266632. https://doi.org/10.1371/journal.pone.0266632.

[36] Acharya, V., *et al.* (2022). Structural insights into the RNA interaction with Yam bean mosaic virus (coat protein) from *Pachyrhizus erosus* using bioinformatics approach. *PLoS One, 17*(7), e0270534. https://doi.org/10.1371/journal.pone.0270534.

[37] Bahaman, A. H., Wahab, R. A., Abdul Hamid, A. A., Abd Halim, K. B., & Kaya, Y. (2021). Molecular docking and molecular dynamics simulations studies on β-glucosidase and xylanase *Trichoderma asperellum* to predict degradation order of cellulosic components in oil palm leaves for nanocellulose preparation. *Journal of Biomolecular Structure and Dynamics, 39*(7), 2628–2641. https://doi.org/10.1080/07391102.2020.1751713.

[38] Rout, A. K., *et al.* (2021). Insights into structure and dynamics of extracellular domain of Toll-like receptor 5 in *Cirrhinus mrigala* (mrigala): A molecular dynamics simulation approach. *PLoS One, 16*(1), e0245358. https://doi.org/10.1371/journal.pone.0245358.

[39] Durrant, J. D., & McCammon, J. A. (2011). HBonanza: A computer algorithm for molecular-dynamics-trajectory hydrogen-bond analysis. *Journal of Molecular Graphics and Modelling, 31*, 5–9. https://doi.org/10.1016/j.jmgm.2011.07.008.

[40] Andrusier, N., Mashiach, E., Nussinov, R., & Wolfson, H. J. (2008). Principles of flexible protein–protein docking. *Proteins: Structure, Function, and Bioinformatics, 73*(2), 271–289. https://doi.org/10.1002/prot.22170.

[41] Mohamad, N., *et al.* (2015). Simple adsorption of *Candida rugosa* lipase onto multi-walled carbon nanotubes for sustainable production of the flavor ester geranyl propionate. *Journal of Industrial and Engineering Chemistry, 32*, 99–108. https://doi.org/10.1016/j.jiec.2015.08.001.

[42] Rahman, I. N. A., *et al*. (2018). Statistical optimization and operational stability of *Rhizomucor miehei* lipase supported on magnetic chitosan/chitin nanoparticles for synthesis of pentyl valerate. *International Journal of Biological Macromolecules, 115*, 680–695. https://doi.org/10.1016/j.ijbiomac.2018.04.111.

[43] Yang, M., *et al.* (2024). A whole-process visible strategy for the preparation of *Rhizomucor miehei* lipase with *Escherichia coli* secretion expression system and the immobilization. *Microbial Cell Factories, 23*(1), 155. https://doi.org/10.1186/s12934-024-02432-y.

[44] Abd Manan, F. M., Attan, N., Zakaria, Z., Mahat, N. A., & Wahab, R. A. (2018). Insight into the *Rhizomucor miehei* lipase supported on chitosan–chitin nanowhiskers assisted esterification of eugenol to eugenyl benzoate. Journal of Biotechnology, 280, 19–30. https://doi.org/10.1016/j.jbiotec.2018.05.015.

[45] Lu, T., *et al.* (2024). Efficient expression and application of a modified *Rhizomucor miehei* lipase for simultaneous production of biodiesel and eicosapentaenoic acid ethyl ester from *Nannochloropsis* oil. *Journal of Agricultural and Food Chemistry*. https://doi.org/10.1021/acs.jafc.4c02360.

[46] Department of Environment. (n.d.). *National water quality standards for Malaysia*.

[47] Sengupta, P. K. (2018). *Industrial water resource management: Challenges and opportunities for corporate water stewardship*. John Wiley & Sons. https://doi.org/10.1002/9781119272496.

[48] Boyd, C. E. (2015). Water pollution. In *Water Quality: An Introduction* (pp. 113–138). https://doi.org/10.1007/978-3-319-17446-4.

[49] Barriuso, J., Vaquero, M. E., Prieto, A., & Martínez, M. J. (2016). Structural traits and catalytic versatility of the lipases from the *Candida rugosa*-like family: A review. *Biotechnology Advances, 34*(5), 874–885. https://doi.org/10.1016/j.biotechadv.2016.05.004.

[50] Rohatgi, R., Sodhi, G. S., & Kapoor, A. K. (2015). Small particle reagent based on crystal violet dye for developing latent fingerprints on non-porous wet surfaces. *Egyptian Journal of Forensic Sciences, 5*(4), 162–165. https://doi.org/10.1016/j.ejfs.2014.08.005.

[51] Wahab, R. A., Puspanadan, J. K., Mahat, N. A., Azman, A. R., & Ismail, D. (2021). Potassium triiodide enhanced multi-walled carbon nanotubes supported lipase for expediting a greener forensic visualization of wetted fingerprints. *Chemical Papers, 75*, 1401–1412. https://doi.org/10.1007/s11696-020-01370-4.

[52] Wang, S., Zhang, P., Xue, Y., Yan, Q., Li, X., & Jiang, Z. (2021). Characterization of a novel aspartic protease from *Rhizomucor miehei* expressed in *Aspergillus niger* and its application in production of ACE-inhibitory peptides. *Foods, 10*(12), 2949. https://doi.org/10.3390/foods10122949.